Development of Quantification Measures to Compare Mechanical and Physical Properties' Patterns from Additive Manufacturing Simulations

Jill Urbanic[1] and Bita Mohajernia[2]

[1]University of Windsor, jurbanic@uwindsor.ca
[2] University of Windsor, mohajerb@uwindsor.ca

Corresponding author: Jill Urbanic, jurbanic@uwindsor.ca

Abstract. Finite element (FE) analysis model results are rich in information beyond their calculated maximum or minimum values. Regional information and patterns can provide additional insights, and in the additive manufacturing (AM) domain, this information provides essential knowledge. AM processes are relatively new and predicting quality and performance characteristics are critical. The goal of this research is to develop tools and strategies to interpret the results data comprehensively. Robust comparison methods to assess different build strategies on the resulting properties for a component are essential for evaluating process planning strategies. Results for residual and von Mises stresses are evaluated using different metrics. For curves, the nearest neighbor and Hausdorff distances are determined along with a repurposed Kolmogorov-Smirnov test. A logic test related to offset curves and a user defined range is introduced. To extract pattern data, the FE images are converted from RGB data into point cloud data using Rhino® and Grasshopper® / VBA tools. The stress levels are binned into z height categories. These points are imported to Excel. Graphs to explore variations between different configurations are readily automated. CAD tools are leveraged to characteristics for selected stress regions. Using image conversion strategies along with CAD tools allows for more in-depth quantified post processing assessments. Although the image conversion strategy has potential, the RGB colors vary within an image, so the conversion from RGB pixel data to valid points is approximately 85% unless manual tuning is performed. It is proposed to use AI tools such as a convolution neural network to reinterpret the noisy regions.

Keywords: Finite Element Analysis, Post Processing, Quantification, Curve Similarity, Shape Similarity Analysis, Additive Manufacturing.
**DOI:** https://doi.org/10.14733/cadaps.2023.898-922

1   INTRODUCTION

Finite element (FE) analysis methods are utilized extensively to explore behaviors of a component or system that cannot be effectively assessed using analytical or experimental approaches. Multiple components, dissimilar materials, complex geometry, and local effects can be included in the model. There is much research related to creating mesh models [6, 7, 21] and strategies to reduce computation time [4, 7, 10, 17]; however, typically, the post-processing analysis of the simulation results tends to focus on identifying maximum and minimum values for the selected mechanical and physical properties in specific regions, not on the intermediate regions or the resulting patterns that occur. There is much data that is not being evaluated, which can provide insights [15]. The goal of this research is to develop tools and strategies to interpret the result data in a structured manner beyond determining maximum and minimum points or querying the properties at specific nodes. The research domain for this paper is in additive manufacturing (AM).

AM layer-based fabrication techniques relatively new and have been developed for several technologies and systems. The metal powder bed processes (e.g., Powder Bed Fusion (PBF) [26]) and the directed energy deposition (DED) processes [2] have different configurations and boundary conditions; however, components fabricated by these processes undergo discrete heating and cooling cycles due to the side-by-side scan paths or deposition tool paths. Robust comparison methods to assess the influence of different build strategies on the resulting mechanical and physical properties of a component is essential for evaluating process planning strategies as well as predicting quality and performance characteristics. For both the PBF and DED AM processes, in-process related information is being captured and evaluated as well as the final results. Consequently, a more comprehensive and quantifiable strategy for comparing build scenario results that assesses the results and the pattern variations between different simulation scenarios needs to be developed.

This research explores curve comparison methods to evaluate localized stress characteristics as well as selected shape and pattern comparisons for different build scenarios. SYSWELD [23] is utilized to generate the FE simulation results. Models calibrated from experimental data have been developed for several DED build scenarios. This includes predicting the hardness and residual stress characteristics for single beads [15], comparing the distortion, hardness, and/or residual stresses for different travel path strategies [13, 19], revaluating the order of operations for junctions [14], and a thin-walled dome [10]. The case studies for this work are illustrated in Fig. 1 to 3. These are extensions of previous research studies. Curves and images for residual and von Mises stress results that highlight the merits of different approaches are evaluated and compared.
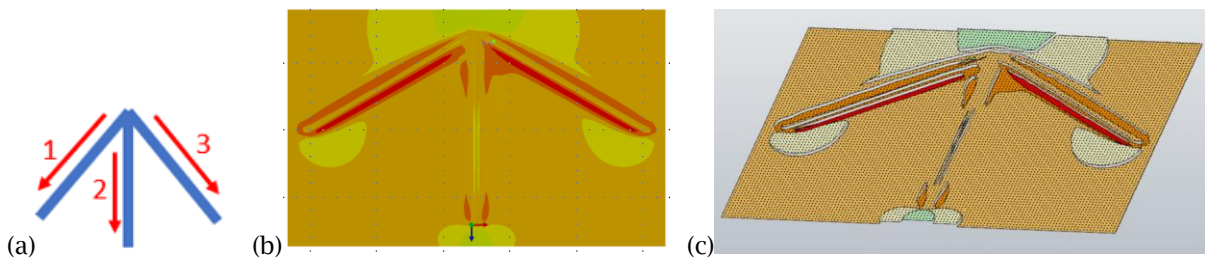
Figure 1: (a) A DED bead set and the deposition order, radiating out from the junction, (b) the FE simulation results for the plate top for the *xx* residual stresses, and (c) CAD model with layers at different z heights which correspond to a *xx* residual stress range, and points for each color-region.
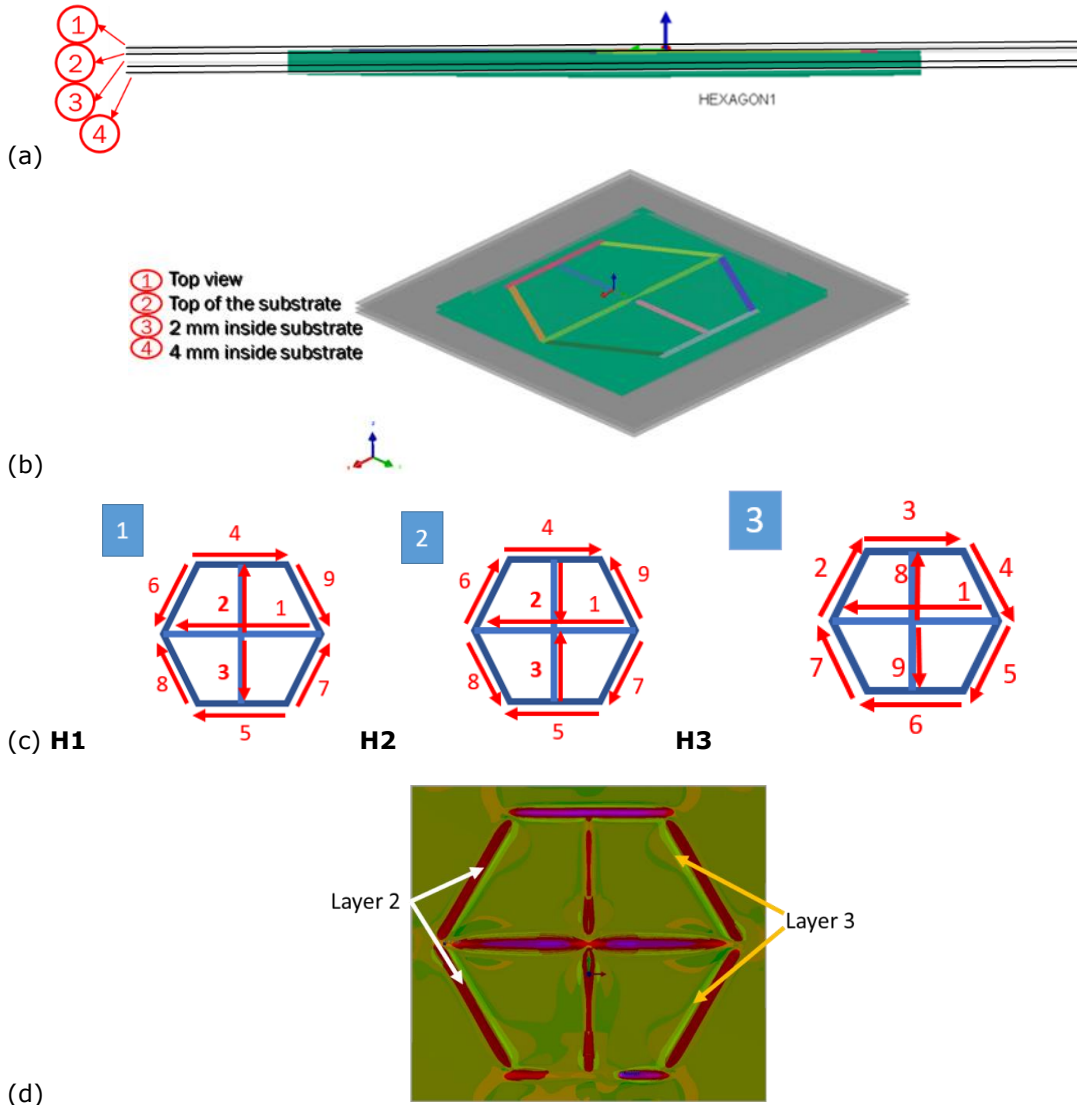
Figure 2: (a) and (b) A hexagon case study, illustrating the reference positions where the images are collected. Note: The Layer 1 top view includes data related to the top of the beads, (c) the three deposition scenarios, and (d) a comparison of the XX residual stresses for the H1 layers 2 and 3 using the GIMP [9] grain extract feature (the red tones represent Layer 2). The shifting residual stress regions between the two layers is noted.

2   BACKGROUND

2.1   Curve Comparisons

The challenge related to comparing curves is not new. As recognized by Alt and Godau [1], developing a metric to determine how curves "resemble each other" is a common problem. They explore using the Hausdorff distance and the Fréchet distance. The Hausdorff distance measures how far two subsets of a metric space are to each other. It is the greatest of all the distances from a point in one set to the closest point in the other set. It is defined as:

(a)

(b)
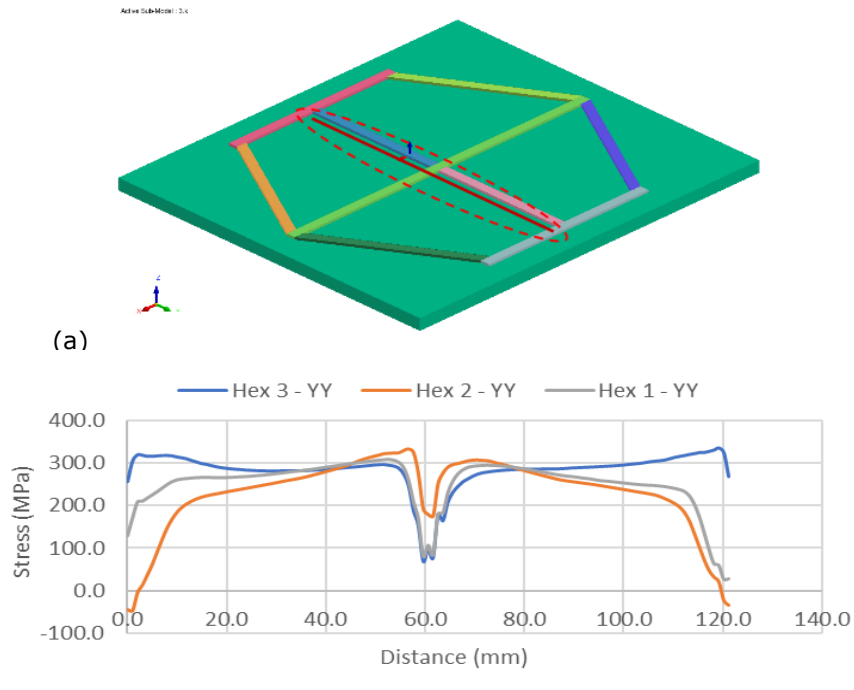
Figure 3: (a) Bead segment with variations in the maximum and minimum YY residual stress values, and (b) the residual stress curves.

$$d_H = max \left\{ \sup_{x \in X} d(x, Y), \sup_{y \in Y} d(X, y) \right\}$$

(2.1)

Where *X* and *Y* are two non-empty subsets of a metric space (*M, d*),
  sup represents the supremum and *inf* represents the infimum, and
  d_H is the Hausdorff distance.

The Fréchet distance considers both the points on the curve and the course of the curve. From Alt and Godau: "Suppose a man is walking his dog, he is walking on the once curve the dog on the other. Both are allowed to control their speed but are not allowed to go backwards. Then the Fréchet distance of the curves is the minimal length of a leash that is necessary."
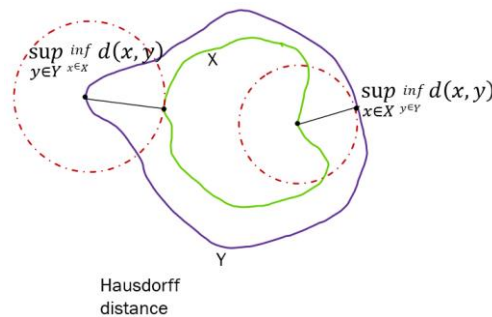
Figure 4: Hausdorff distance.

The two concepts complement each other: the Hausdorff distance is a 'maximum-minimum distance' and the Fréchet distance is a 'minimum-maximum' distance. The discrete Fréchet distance is computed when comparing point lists (Fig. 5 (a)). The endpoints 'of the leash' are located at the vertices of the curve. For the complete sets of points, the Fréchet distance equals the Hausdorff distance [5]. The Fréchet distance may be an important metric for cartography or character recognition, but not for this research. Here, the Hausdorff distance and the nearest neighbor distance (NN), the minimum distance between two curves, is utilized (Fig. 5). It is clear that the NN distance cannot be assumed to be the minimum Δy value.
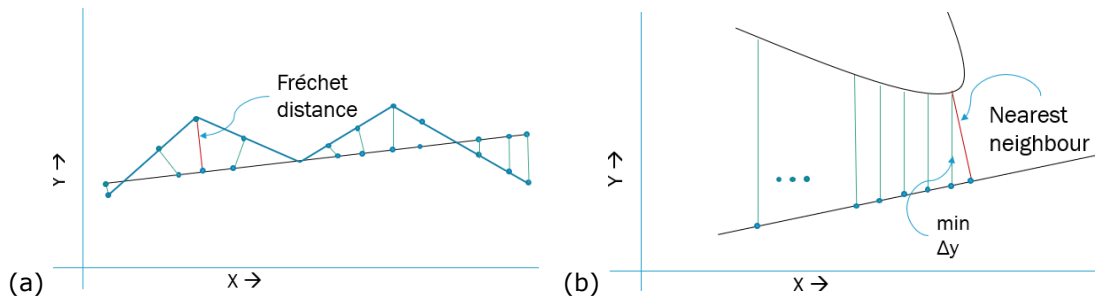
Figure 5: (a) The Fréchet distance, and (b) Δy distance calculated for each x point compared to the nearest neighbor.

Another approach to consider is comparing cumulative sums, and then calculating the maximum distance between those curves. The smaller the dissimilarity, the more the curves are similar. This is a simplified version of the Kolmogorov-Smirnov (K-S) test used to compare a sample's distribution to a reference probability distribution. The cumulative sum is defined by [22]:

$$x = [x_1, x_2, x_3, \ldots, x_N] \tag{2.2}$$

$$y = [x_1, x_1 + x_2, 10x_1 + x_2 + x_3, \ldots, x_1 + x_2 + x_3 \ldots x_N] \tag{2.3}$$

$$y_N = \sum_{i=1}^{N} x_i \tag{2.4}$$

Where x is an array of data points
       y is an array of cumulative sums, and
       i is an index, and N is the maximum number of values to be considered.

At each point i the difference between the cumulative sums for the reference curve and the curve are calculated, and this list of difference values is evaluated. Cumulative sum curves are illustrated in Fig. 6. Although concerns have been raised with respect to signed distances for evaluating statistical distributions [8], the focus is not on determining the nature of a random sample and its statistical distribution in this work, so this is not a factor to be considered.

To summarize, these curve assessment tools provide a discrete distance value, which provide a basis for relative comparisons between curve sets, but an absolute assessment method to evaluate curve pairs should be developed. When performing statistical analyses, tolerance intervals allow for sample set data to be evaluated for a confidence level. A variant of this approach has been utilized to assess relative errors when the true value is zero (and example is shown in Fig. 7), and has eliminated distortion issues [19]. Therefore, the Hausdorff distance, NN, modified K-S test, and a novel 'tolerance interval' inspired approach, based on offset curves, are derived and the results compared.
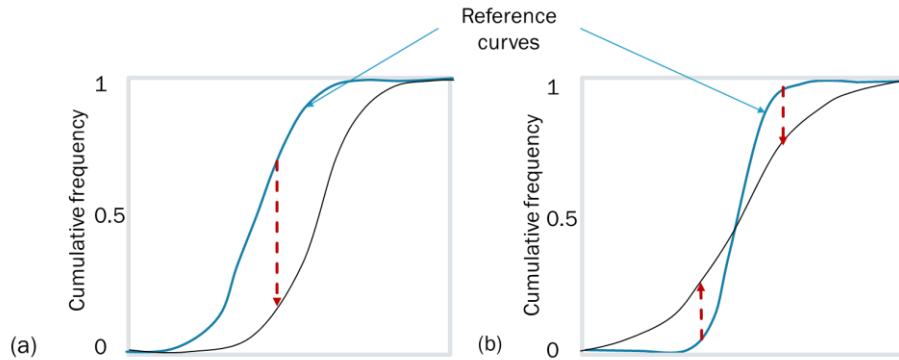
Figure 6: (a) Distributions that have different locations, and (b) distributions that have different variances, adapted from [8], however, for this work, the maximum distance between the curves is being determined.

2.2 Shape or Pattern Analyses

There are identifiable patterns that are generated as results for an FE simulation. Pattern analysis or similarity measures should be introduced to quantify characteristics or provide baseline classification information for a given result set to allow researchers to compare results systematically. Data extraction from images must be performed prior to shape or pattern analyses.

2.2.1 Data Extraction

There are many tools available to convert greyscale image data into a point cloud data set, a mesh, or a surface, where the x, y values correspond to the pixel positions, and the z height is related to the grey scale value. Utilities within Rhino®, and other software packages typically utilized for design and manufacturing (i.e., Mastercam®) have this ability. The issue with this grey scale mapping is that distinct colors may transform into very similar grey scale values (Fig. 8(b)). Therefore, distinct regions (here the residual and von Mises stresses) cannot be automatically classified in a controlled and repeatable manner. Consequently, in previous related research, Urbanic et al. [25] developed semi-automatic methods to convert image data into geometry where the z coordinate corresponded to a specific stress value, which in turn could be exported as a .txt or .csv file.

This is a standardized platform-independent method for generating data sets from FE simulation results. An example is presented in Fig. 9. for three parallel beads deposited using different process settings, and Fig. 10 for a three-bead junction scenario.

Although this approach provides data classifications that lends itself to additional data analyses, as shown by the Excel conditional formatting representation of the images, this semi-automatic methodology is problematic for collecting data for complex patterns, such those for the von Mises stresses shown in Fig. 8 (a). It can be seen that there are several complex curves that collapse or intertwine (Fig. 11 (a) and (b)). Consequently, there are problems with boundary curve generation and extruding operations. It is proposed to exploit image manipulation tools, where classifications are defined for the distinct colors identified in the FEA results legend (Fig. 8 (a)) and developing a targeted image sampling strategy. In lieu of developing z height due to grey scale values (Fig. 8 (b)), the z height values will be assigned by an RGB-stress levels classification strategy.
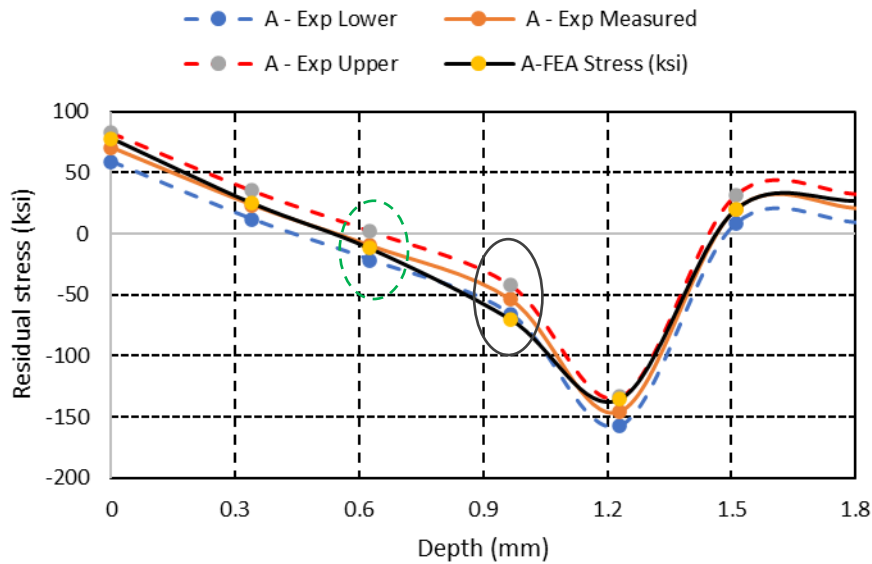
Figure 7: A comparison of the FEA solution to the experimental residual stress data, where five of six evaluation points are within the experimental upper and lower bounds [19]. A point near zero is enclosed with a dashed ellipse. The outside point is enclosed with a solid ellipse.
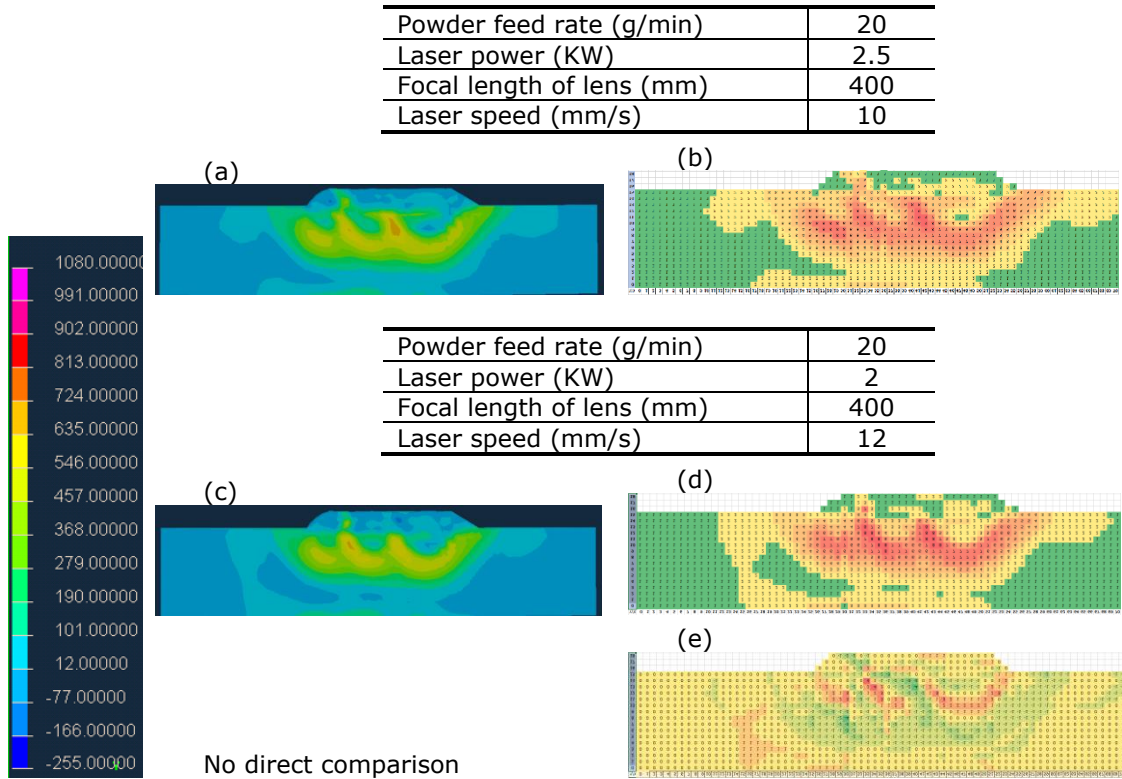

(a)   (b)
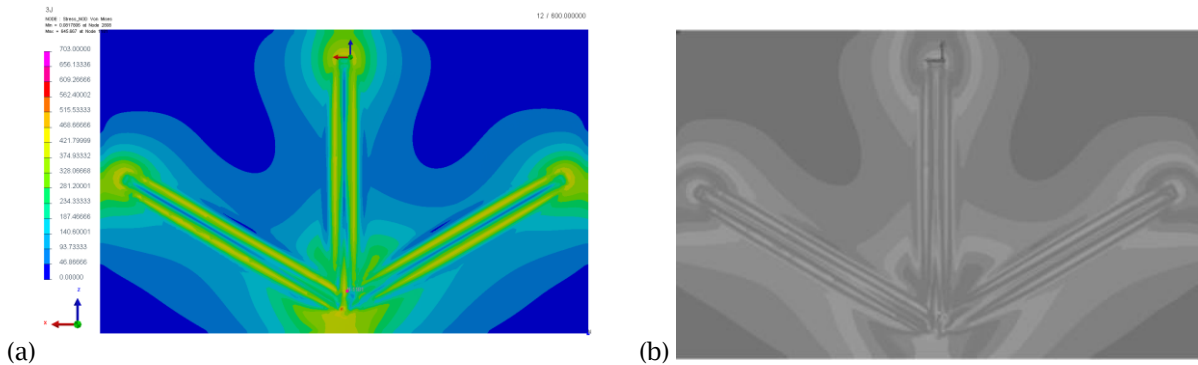
Figure 8: The von Mises stress patterns for the model shown in Fig. 10, where (a) is stress pattern at the top of the plate, (b) the grey scale representation.

2.2.2   Shape Recognition Background

There has been much research on shape recognition and human perceptions of shape similarities between objects [12, 16, 18]. This includes assessing scale changes, translations, and rotations. Shape similarity measurements are usually used for shape matching and indexing for databases, transmitting geospatial data [24], and for psychological cognition [16]. To search for similarity between polygons, Kaplan et al. [11] analyze the line segment lengths and the angle between segments via turning functions, which is an interesting approach; however, it is a localized approach. Much research has been done with respect to shape recognition, but at this time, there appears to be no tools for quantified FE result comparisons.

Powder feed rate (g/min)	20
Laser power (KW)	2.5
Focal length of lens (mm)	400
Laser speed (mm/s)	10

Powder feed rate (g/min)	20
Laser power (KW)	2
Focal length of lens (mm)	400
Laser speed (mm/s)	12

No direct comparison

Figure 9: (a) & (c) Residual stress results for 40% overlap for the presented process setting (b & (d), the heat map, and (e), the difference map for the two FE simulations, adapted from [25].
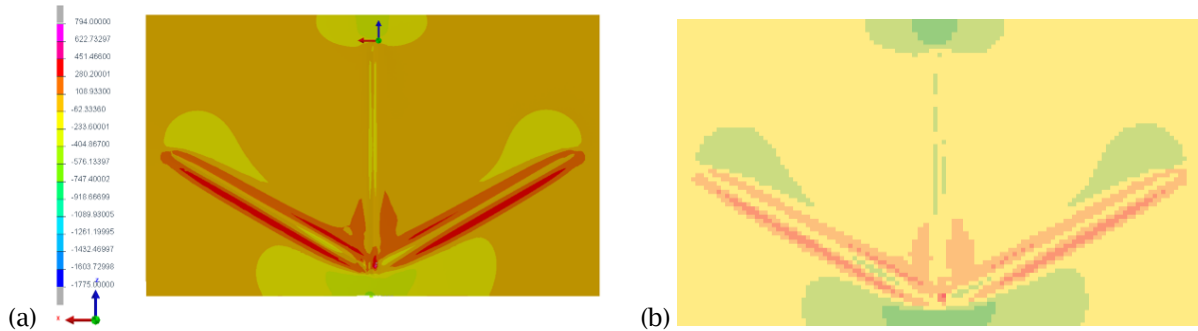

Figure 10: (a) The original results for the FE model [14] (radiate into the junction case), (b) an Excel representation of the data points using conditional formatting to illustrate the different z heights-stress values.

The extracted point cloud data sets allow for direct comparisons between build scenarios to be performed from multiple perspectives. Analyzing the data samples using basic difference evaluations and statistical tools on the global data set can provide global and local information. In Fig. 9 (e), a difference map is illustrated showing regions where the residual stress levels are higher or lower between the three bead build configurations. A graph enumerating the cells and

the resulting the stress level quantities for each stress level bin is shown in Fig. 12 for two build scenarios.

(a)   (b)
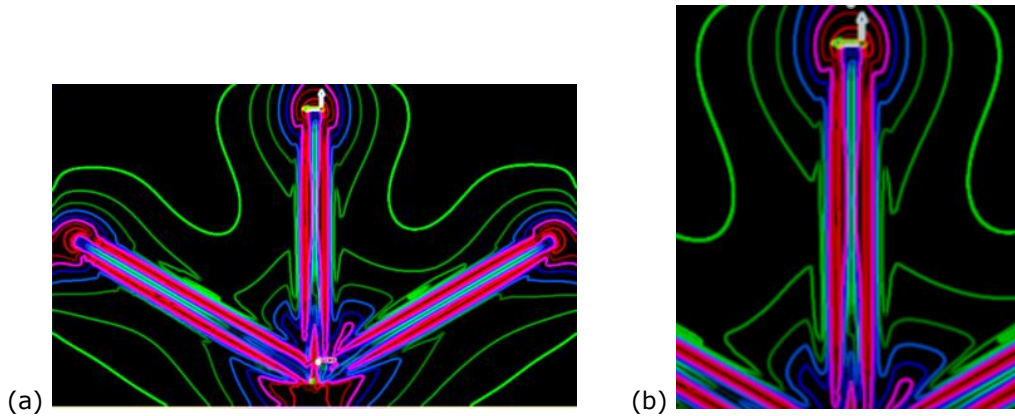
Figure 11: The von Mises stress pattern boundary curves using GIMP for the model shown in Fig. 10, where (a) illustrates the complete results and (b) illustrates an expansion of the centre bead showing complex overlapping regions.
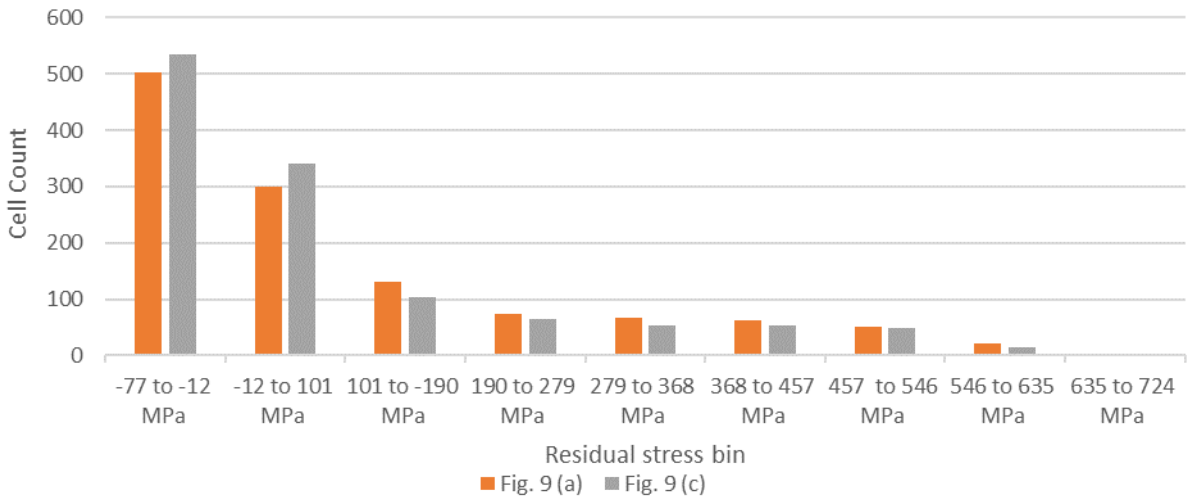
Figure 12: Residual stress bins data for the two simulation scenarios presented in Fig. 9. Note that the build conditions in Fig. 9 (a) have less compressive stress cells (503 vs 534) and more high tensile stress cells (4 vs 0).

Manipulating the FE model-based point cloud data provides unique opportunities. Employing CAD and Excel tools enable the patterns and shapes derived from the FE simulations to be quantified for absolute and localized regions. Unlike shape similarity assessment strategies used for object localization [16], algorithms to match and recognize 2D objects [3], or strategies to analyze cell populations [20], at this time the user is to define the regions of interest for analysis, and the baseline shape sets for comparisons, as described in the next section.

3   METHODOLOGY

3.1   Curve Analysis

To analyze and compare curve sets, a combination of statistical and geometric analyses is conducted. Basic statistical analyses are utilized to determine the average, minimum, and maximum values, and the ranges for each curve being considered. The nearest neighbor (NN), Hausdorff, and the Kolmogorov-Smirnov (K-S) test distances are determined between curve sets using Excel functions. This provides the minimum and maximum distance data between a reference curve and the ones being compared from different perspectives.

To develop a measure of closeness based on the complete curve data, an offset curve capture (OCC) logic test is developed. For the reference curve, offset curves are derived using standard CAD functions. The offset values are determined as a percentage of the range. An 'In-Out' TRUE-FALSE logic test is performed for each point on the comparison curve, and the percentage of the 'TRUE' data points is calculated.

Parametrized curve sets are explored, as a parametric representation will be insensitive to scaling and curve shifts. The curves are parametrized between [0, 1] as presented in eqn. 3.1:

$$x\_parm_i = \frac{(x_i - x_{min})}{(x_{max} - x_{min})}, x\_parm \in [0, 1]$$

(3.1)

Where x is a value to be parametrized, and i is an index

X_{max} is the largest number,

X_{min} is the smallest number of the data set to be parametrized, and

X_parm_i is the parametrized value, between 0 and 1

3.2   Point Cloud Data Extraction

Point cloud data extraction cannot be performed directly from an image as conventional topology creation solutions in Rhino© (or other image to CAD conversion software tools) utilize grey scale (or one-color channel) data. Therefore, Rhino© with Grasshopper© is utilized along with VB scripts to analyze an image and transform the image red (R), green (G), and blue (B) color values into 3D point clouds, where the x, y values are positions on the image, and the z value is related to a color that is associated with a displayed stress level. Using Rhino© + Grasshopper© tools, data is manipulated or isolated to allow for subsequent downstream analyses. The process flow and tools are presented in Fig. 13 and are summarized as follows.

- In any image software (i.e., GIMP), analyze select pixel data for each color region to determine RGB color values. The average values and a range need to be determined. Associate the RGB values with the stress level classifications.
- In Grasshopper:
  - o   Create a grid of data points.
  - o   Analyze the image and transform the RGB data for each grid point into the desired classification value.
  - o   Construct a 3D point cloud where the z value corresponds to a specific stress classification value.
- In Rhino®:
  - o   Create curves for filtering / isolating key regions.
- In Grasshopper:
  - o   Filter the data, and / or
  - o   Perform image difference operations.
  - o   Output *x,y,z* data into Excel or other data analysis tools.
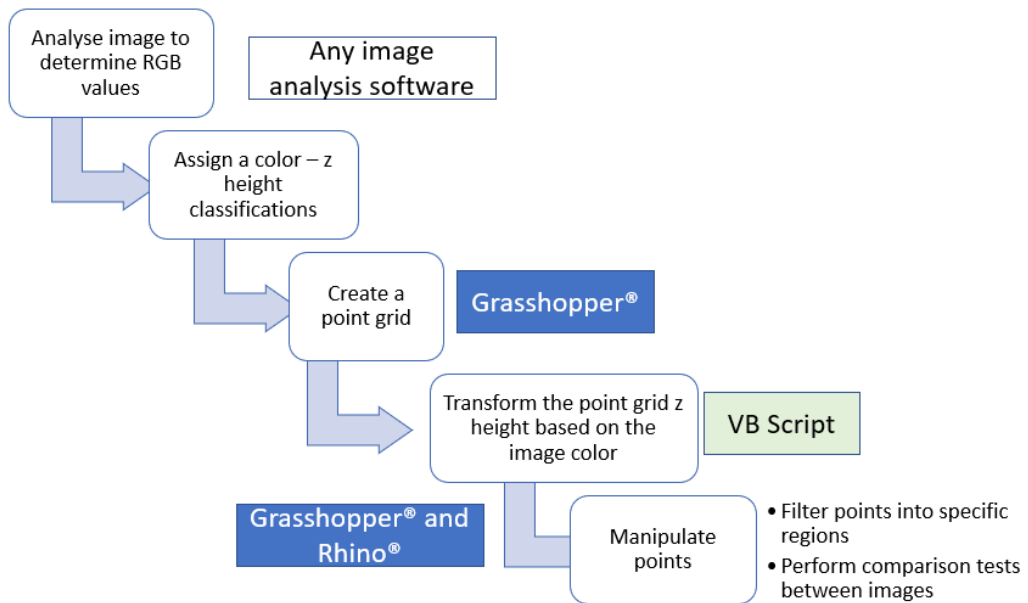
**Figure 13:** Image to geometry transformation process flow.

3.3 Pattern Analysis

The shape and pattern analyses are conducted from two different approaches. The first approach consists of using the point cloud data within Excel to isolate and evaluate regions. Surface graphs with conditional formatting are used for illustrations. Global and local comparisons are conducted via Excel logic, mathematical, and statistical functions, and are graphed. Standard templates are created to facilitate the assessments of different build scenarios, the observed asymmetry of stress patterns within a sample, and the stress variations at different depths. Sample templates are presented in Fig. 14, where selected classification values can be extracted across the complete data set (Fig. 14 (a)), for isolated regions (Fig. 14 (b)), or for filtered data (Fig. 14 (c)).

Rhino® CAD tools and Grasshopper® are utilized for the second approach. Shape analyses based on geometric descriptors such as the contour perimeter, the area, and the centroid positions are performed. Complementing the curve analysis approaches, for sets of shapes overlayed on each other, the Hausdorff distances, the intersection ($\cap$) and union ($\cup$) areas, and the percentage of the intersection area compared to the union are analyzed. Understanding the shifts in centroid positions, and size variations for the residual stress patterns from one layer to another or one deposition scenario to another may provide insights for predictive modeling.

4 RESULTS

Investigations with respect to reframing the simulation strategy for multi-layer scenarios are being conducted. Selected residual stress curve comparisons to evaluate the influence of the tool path and the order of operations is presented as well as the influence of different modeling strategies. When reducing the AM simulation problem space, rigorously assessing the goodness of a different modeling configuration is required.
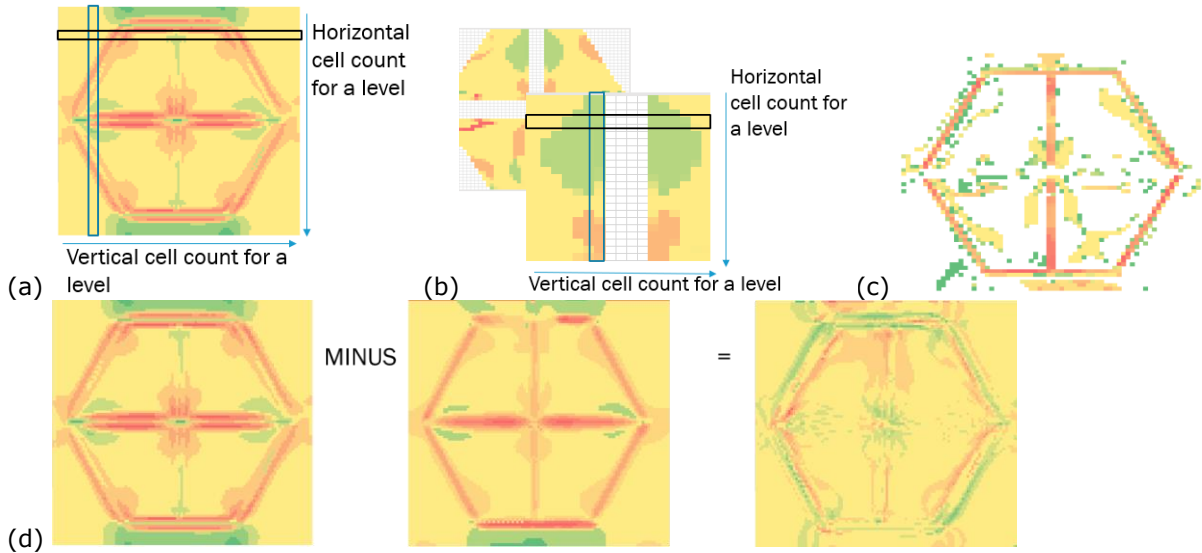
Figure 14: (a) Absolute data set counts for each classification (b) targeted data set counts for the 'green' classification, (c) filtered data illustrating targeted classifications, and (d) illustrates a stress difference map comparing two build scenarios (H1 and H2).

4.1 Curve Analyses Results

In Fig. 15, section A-B for the XX residual stresses is presented for the case studies shown in Fig. 2 (c), where different deposition strategies are employed. The average values for the H1, H2, and H3 residual stress configurations are -605, -558, and -534 MPa respectively. There are regions where the H2 results are closer to the H3 results, and where the H2 results are closer to the H1 curve (Fig. 15 (b)). The NN distance and the K-S test (Fig. 15 (d)) values presented in Table 1 clearly show that H2 is closer to H3, but the smallest Hausdorff difference is between curves H2 and H1. The difference between evaluating the Δy values versus the NN distance is also shown. The minimum distance evaluation depends on the metric being employed.

Minimum Δy values (MPa)			Hausdorff distance (Δy values) (MPa)		
Distance H2-H3	Distance H2-H1	Distance H3-H1	Distance H2-H3	Distance H2-H1	Distance H3-H1
2.4	18.7	11.0	94.6	**72.2**	114.5
Nearest neighbor distance (MPa)			K-S test results (MPa)		
NN Distance H2-H3	NN Distance H2-H1	NN Distance H3-H1	Difference H2-H3	Difference H2-H1	Difference H3-H1
1.0	1.4	1.3	**581.8**	1097.1	1633.1

Table 1: A summary of the similarity evaluation distances for the XX residual stresses.

For the YY stress curves illustrated in Fig. 3, the metrics are summarized in Table 2. As the curves cross, the minimum and NN distance values should be zero, but are not as discrete points are being evaluated. For this case, the H2 and H1 stress curves are closest based on the Hausdorff and K-S test results.

| Minimum Δy values (MPa)			Hausdorff distance (Δy values) (MPa)		
Distance H2-H3	Distance H2-H1	Distance H3-H1	Distance H2-H3	Distance H2-H1	Distance H3-H1
0.1	0.8	0.1	350.3	**217.2**	297.8
Nearest neighbor distance (MPa)			K-S test results (MPa)		
NN Distance H2-H3	NN Distance H2-H1	NN Distance H3-H1	Difference H2-H3	Difference H2-H1	Difference H3-H1
0.1	0.8	0.1	6097	**2361**	3998

Table 2: A summary of the similarity evaluation distances for the YY residual stresses for Fig. 3.

(a)

(b)

(c)

(d)
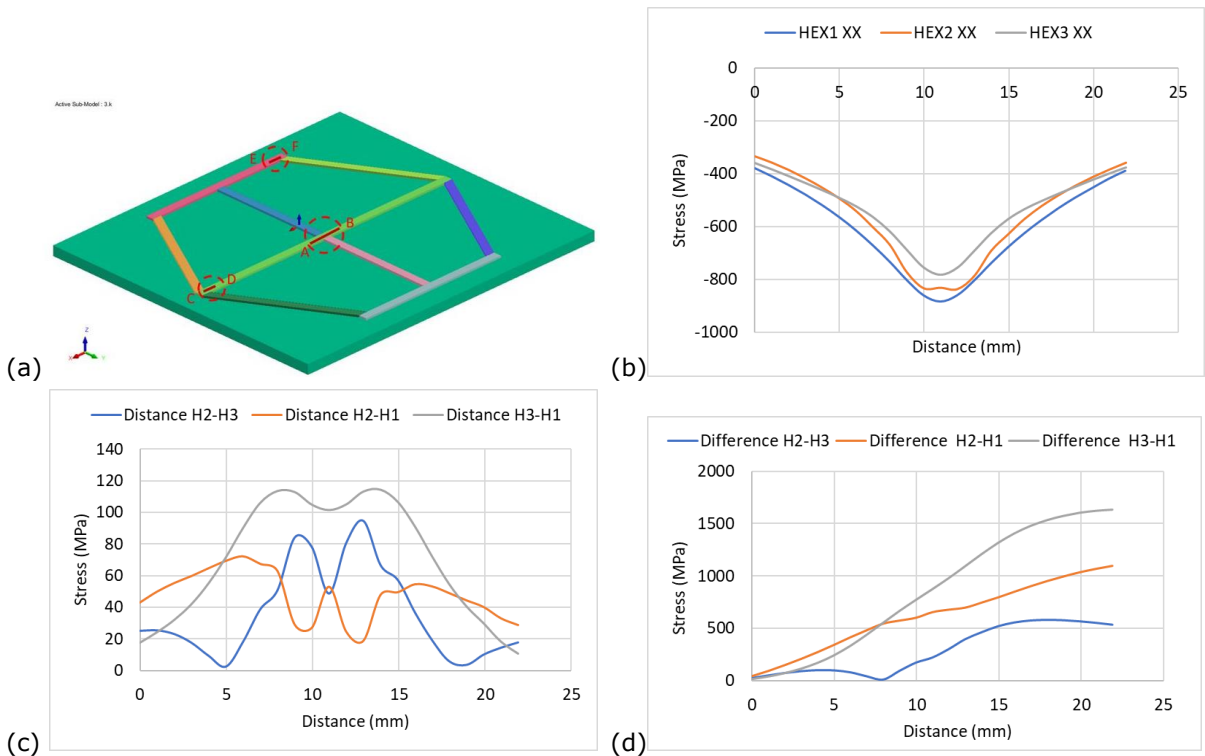
Figure 15: (a) A-B curves on top of the bead are represented, where (b) is the XX residual stress data, (c) are the difference curves, and (d) is the cumulative sum for each difference data set.

Instead of using a transient moving heat source, an imposed thermal cycle can be introduced [23]. This can reduce the computation time significantly. Although the transient and imposed thermal cycle stress curves in Fig. 16 (b) appear to be close visually, this must be validated. The data is trimmed at the beginning and end of the von Mises stress curve data sets to eliminate the mathematical transient conditions. The calculated values for the two data sets are summarized in Table 3. The averages of the two curves are very close, with only 2 MPa as the difference, but the Hausdorff value (@ 142 mm position) is 186 MPa. The curves cross, so the NN non-zero values are due to the discrete data lists. The results in Table 3 are difficult to contextualize as there are only

two curves. When offsetting the transient curve by 10% (Fig. 16 (d), 82% of the imposed thermal cycle data is within this bounded region. When changing the offset to 15%, this increases to 90%, but a 5% offset reduces this value to 29%. Although the average values of these two data sets is close, the OCC percentage results show that there is variability between the two curves. However, based on these assessments, it can be quantitatively stated that the results for the two modeling strategies produce similar von Mises stress results.

(a)

(b)

(c)

(d)
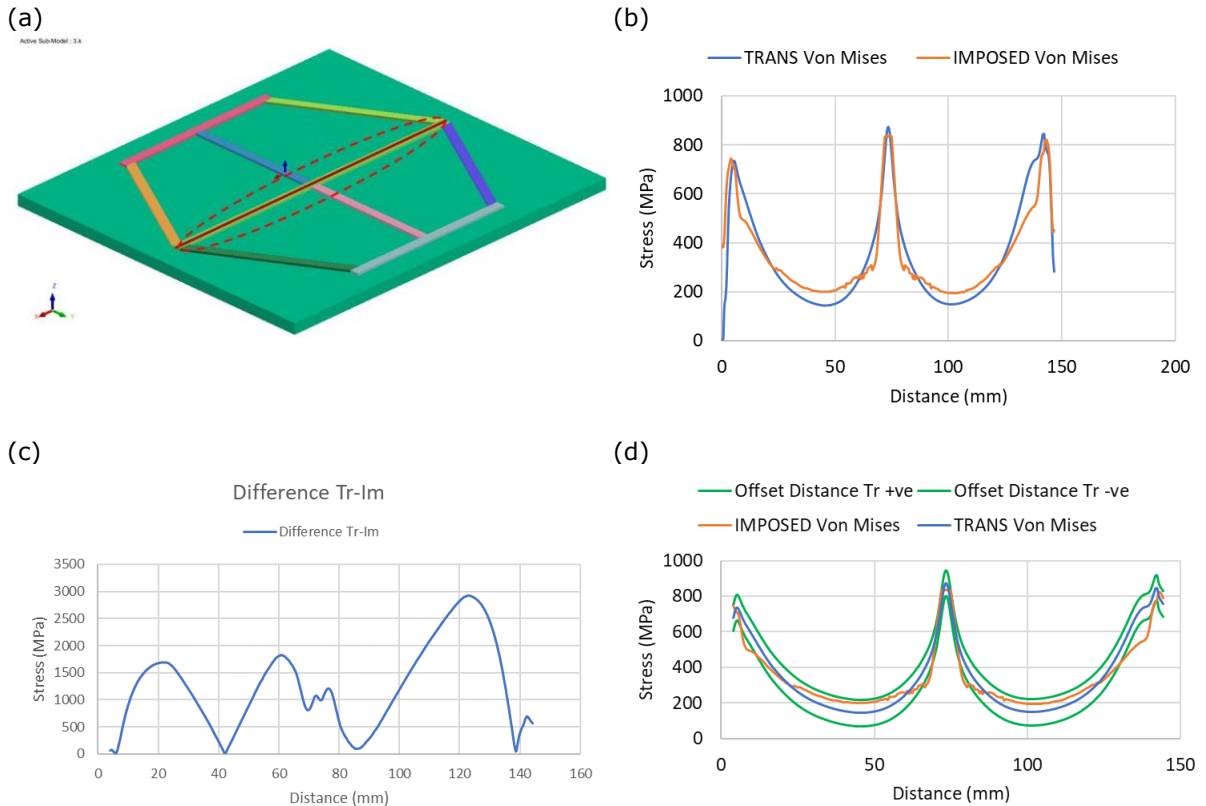
Figure 16: (a) The segment being evaluated with the trimming reference lines, (b) the von Mises stresses, (c) the cumulative sum differnce curve, and (d) the offset curves.

Parameter (Trimmed)	Value (MPa)
Average Trans	345
Average Imposed	343
Min ΔY Distance	0.75
NN Distance	0.60
Hausdorff Distance	186
K-S Max Distance (Fig. 16 (c))	*2927*

Table 3: Parameter summary for assessing the difference between the transient and imposed thermal cycle von Mises stresses.

For multi-layer build scenarios, heat is accumulated. A question on whether a pre-heat scenario could be similar to that of a deposition-based simulation model is explored. For the H3 configuration, a 5-layer model is simulated. A pre-heat is applied to layers 1 – 3, and two

additional deposition layers modeled. This is compared to the full 5 layer simulation model by assessing the resultant von Mises stresses (Fig. 17). The curve similarity distance parameters are presented in Table 4.

The K-S value for this case is 38 times greater than the transient-imposed thermal cycle case. The Hausdorff distance is almost twice the average preheat stress value. The OCC percentage indicates that there is no overlap with a 10% offset. This is true for a 15% offset as well. These curves are not similar, and it can be quantitively stated that a preheat conditions introduce unique resulting stresses. Exploring preheat conditions will be a separate research activity.
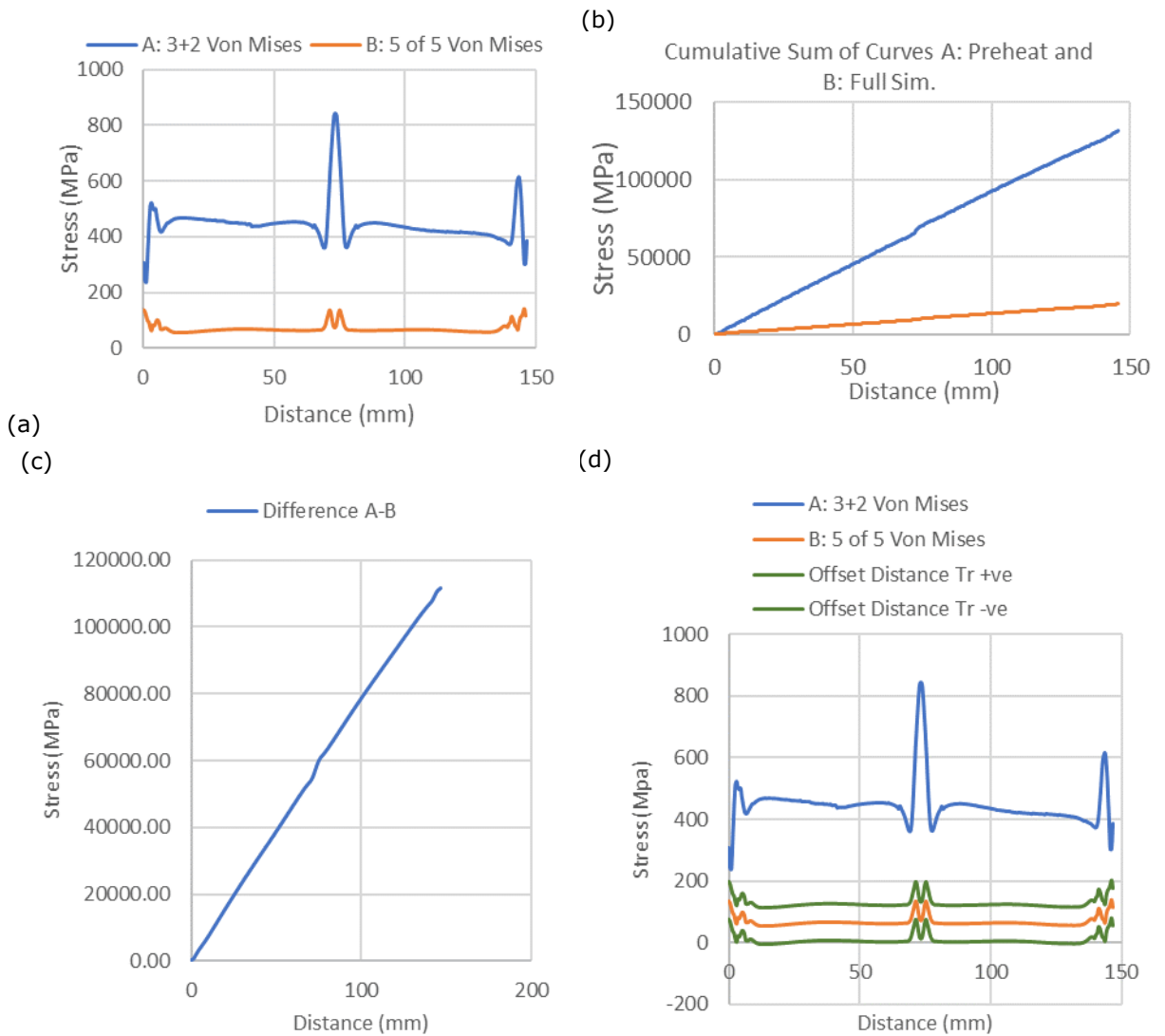
Figure 17: (a) The von Mises stresses, (b) the cumulative sums for each scenario (c) the cumulative sum differnce curve, and (d) the offset curves.

Parameter	Value (MPa)
Average Preheat	446

Average Full Sim.	67
Min ΔY Distance	112
NN Distance	102
Hausdorff Distance	773
K-S Max Distance (Fig. 17 (c))	*111,677*

Table 4: Parameter summary for assessing the difference between a preheat initial condition and a full simulation on the von Mises stresses for the top layer.

4.2 Curve Similarity Analysis Discussion

The average value differences, combined with the NN, Hausdorff and K-S Max distance values provide insight to a curve set's similarity. However, these metrics do not always result in the same answer. These various distance metrics are sensitive to curve peaks and valleys. When assessing sets of curves (Fig. 15), or comparing results between case studies (Fig. 16 and 17), the NN, Hausdorff and K-S Max distance provide a good quantitative relative basis of comparison. For a general curve pair, those metrics have limited value.

The OCC percentage metric is a relatively simple strategy to provide a similarity value, and it is meaningful for assessing similarity between two curves, as well as curve sets. However, the algorithms developed for CAD tools need to be employed to create valid offset curves in a data manipulation package. Point projection must be used to ensure that the original Δx values are maintained. The offset curves are compressed and appear to be translations in y, but this is a graphic artifact. Fig. 18 expands a region to illustrate the offsets.
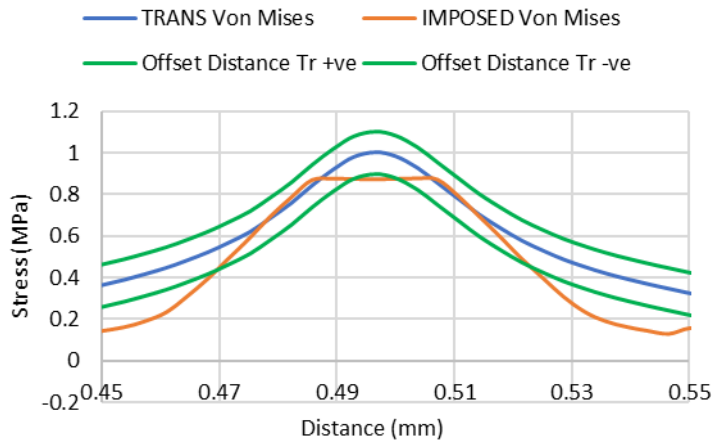

Figure 18: Offset curves for Fig. 19.

For the Fig. 15 results, the influence of shifting and parameterizing the curves is explored. These variants are presented in Fig. 19. The cumulative sum curves are significantly impacted, but as expected the K-S Max distance for the shifted curves is identical as the values reported in Table 3. The OCC percentage results remain consistent as it should for this case as well as for uniform scaling scenarios.

Mean shift case study   Parametric curve case study

(a)   (d)
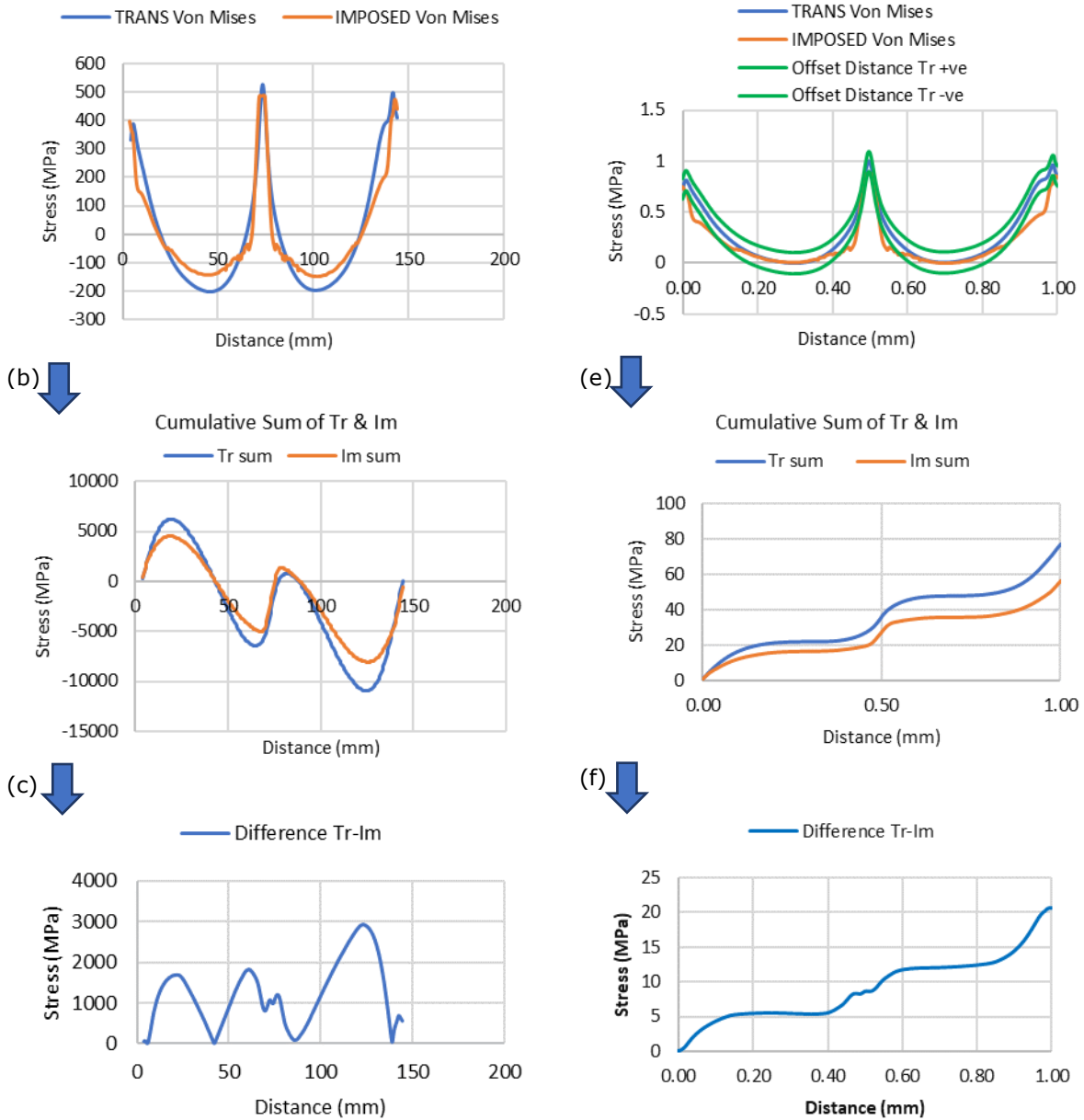
Figure 19: Mean shift case study (a) the von Mises stresses, (b) the cumulative sums (c) the cumulative sum differnce curve; the parametric curve case study (d) the von Mises stresses with offset curves, (e) the cumulative sums (f) the cumulative sum differnce curve.

Parametrization introduces a distortion. The cumulative sum curves, and the location of the K-S maximum distance point, is different as well as the K-S maximum distance value. It was unexpected that the location of the maximum K-S distance would change. The parametrization also influences the OCC percentage values. The comparison curve within the 10% offset region from the reference curve is 67%, and 80% for a 15% offset for the Fig. 19 (d) curve set.

## 4.3 Image Data Extraction and Analyses Results

Two main strategies are utilized to evaluate the FE image patterns: (i) chart-based evaluations in Excel (ii) and geometric analyses. With a point cloud with a specific x, y grid, template files can be readily developed, and seeded with discrete data (Fig. 20).

(a)　　　　(b)　　　　(c)　　　　(d)
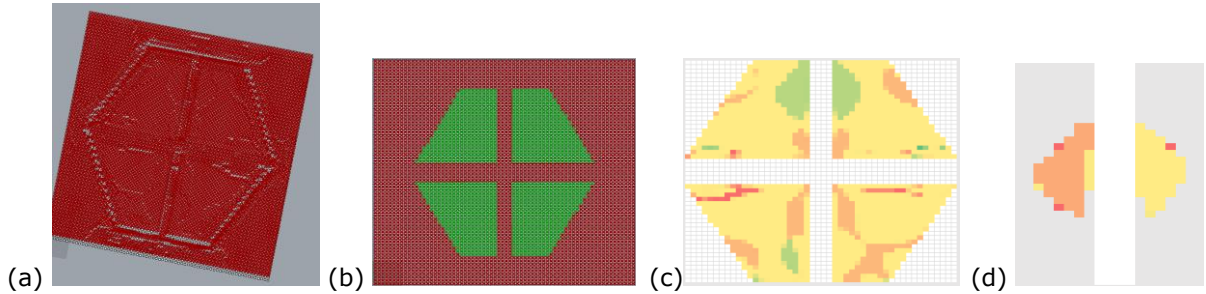
Figure 20: (a) XX stress differences between H1 and H3, (b) filtered data for key regions (green), (c) Excel data representation (using Excel conditional formatting), and (d) the variations in stresses for a targeted region (using Excel conditional formatting to highlight differences).

The blue dot represents position 1 for both the 4-sided polygon defining the regions of interest (Fig. 21 (a)) and the start point when comparing the encircled stress patterns (Fig. 22 (a)). In Fig. 21, the orange cells (identifying low to no stress regions) are enumerated using the Excel COUNTIF function in the vertical direction.

The differences in stress regions vary significantly between quadrants Q2 and Q3. It is evident visually, but the Fig. 21 (b) graph quantified these differences for the low stress regions common for the H1 and H3 simulations (orange).

(a)　　　　(b)
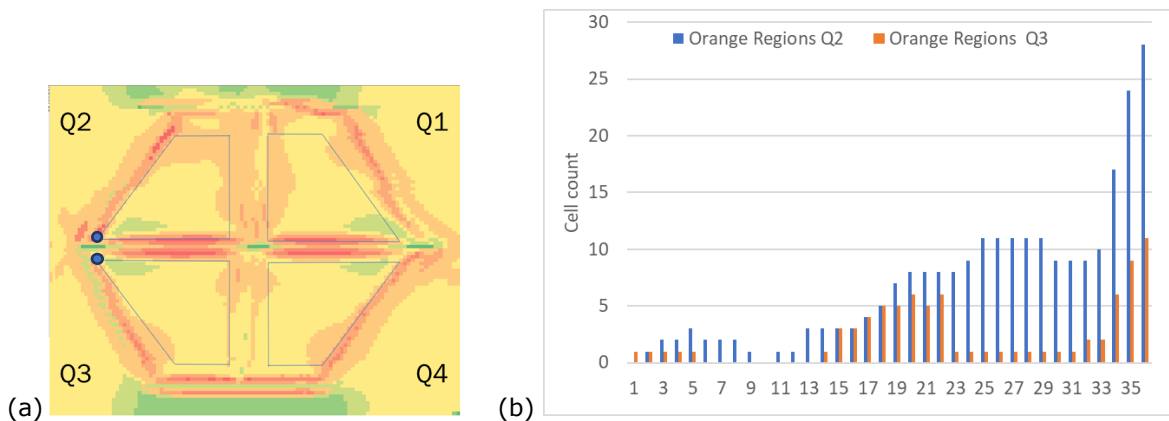
Figure 21: (a) Trapezoid base shapes identifying the regions to be assessed for H1, (b) a comparison of the number of 'orange' cells along the horizontal axis with residual stress level 4 (-99 to 6 MPa).

In Fig. 22, the residual stress levels from the filtered data from Fig. 14 are illustrated. The shape differences for the green regions in Q1 and Q2 are shown in Fig. 22 (b). Assessments on the complete data set for are shown in Fig. 22 (c), where the different stress level percentages are summarized for each quadrant.
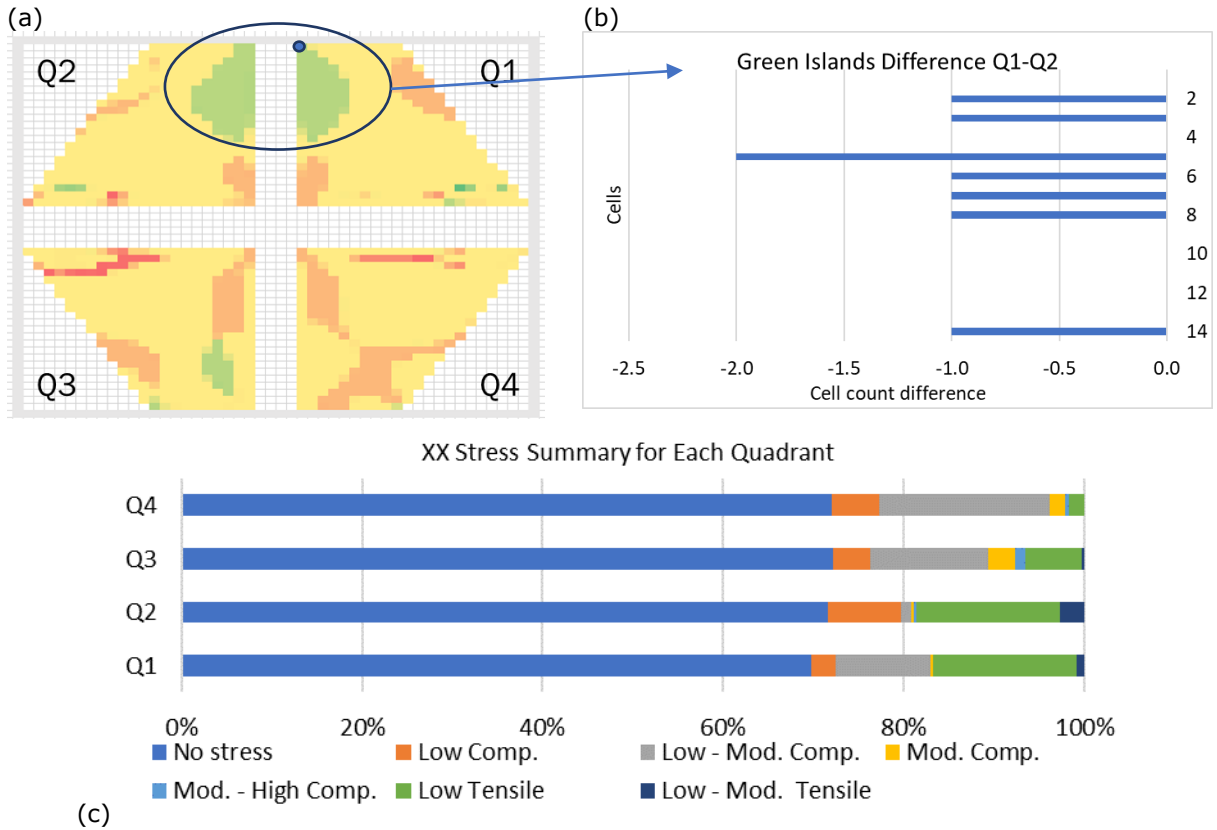
Figure 22: (a) XX stress differences when comparing the H3 to H1, (b) a bar chart illustrating the differences in the encircled region, and (c) a stress level difference summary for each quadrant.

Radar charts visualize differences in symmetry as shown when comparing the XX residual stress levels differences between the H1 and H3 configuration at the top of the plate (Fig. 23 (a)).

Line graphs illustrate the differences in stress levels for the 3-joint radiate in and radiate out configurations at the top of the plate, and 4 mm into the plate. For both configurations it can be seen that the center branch region has the greatest variability for comparisons. The range is very high for the in-plate situation. Overall, however there are less change in the stress levels 4 mm into the plate (Fig. 24). The statistics validate this observation, as shown in Table 5.

|	Top: 1 level+	Top: 1 level -	In plate: 1 level+	In plate: 1 level-
Average cell count	5.4	4.5	3.2	2.3
Range	26	33	33	42
Stand. Dev.	4.3	3.8	3.6	4.1

**Table 5:** Statistical summary for Fig. 24.
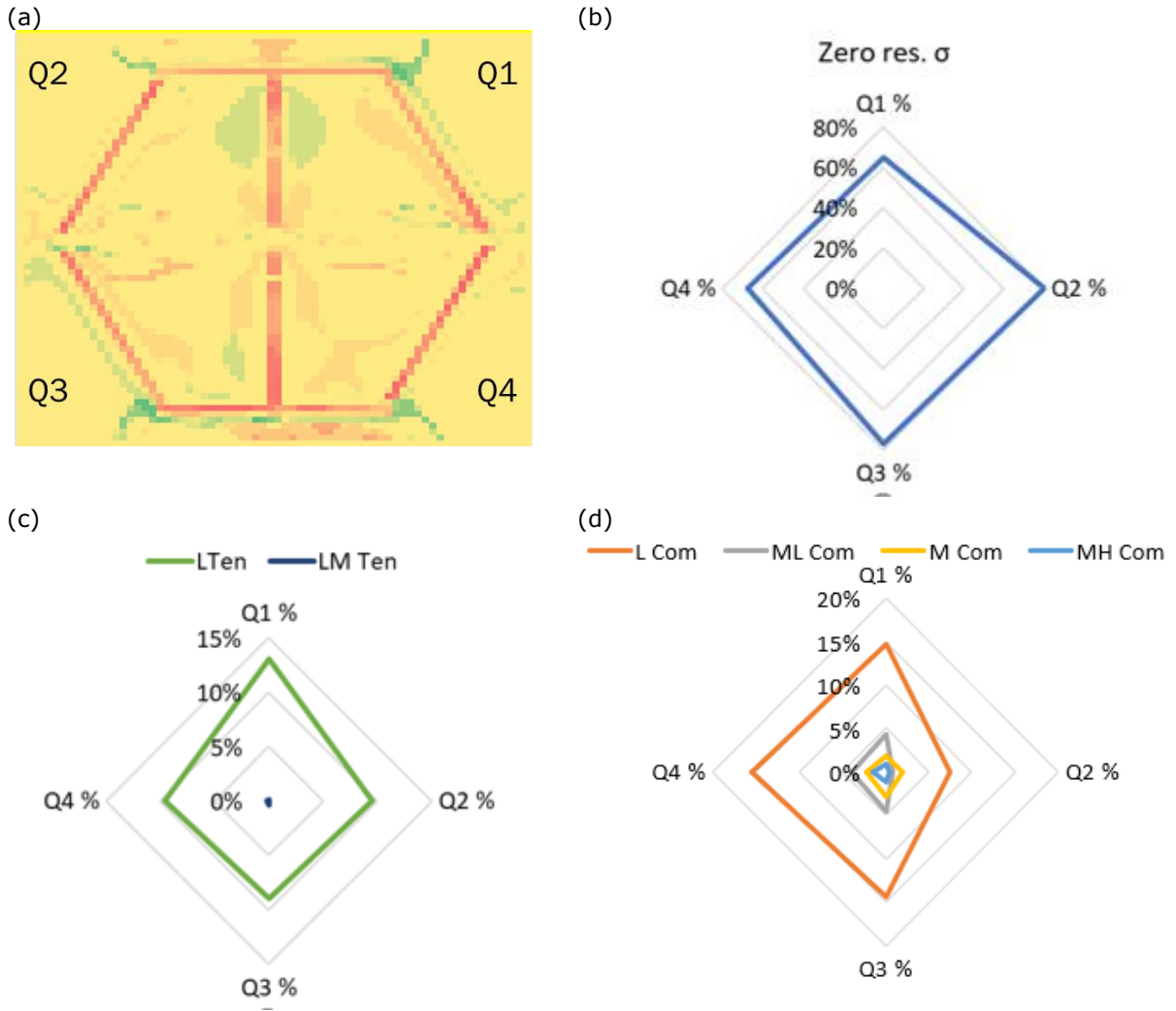
Figure 23: (a) Difference in the XX stresses at the plate top for the H3 and H1 configurations, (b) radar graph illustrating the percentage zero σ differences between the two build scenarios, (c) and (d) the difference of the tensile and compressive stress levels for each quadrant.

The characteristics of regional and global stress patterns within a sample, between samples, at different depths within a sample can be represented from different perspectives. Relating the discrete cells to geometric values, this trend data can be transformed into area values. Gradient data can also be extracted. Geometric analyses for select regions is presented next.

In Fig. 25, the asymmetry of the low von Mises stress regions for the H1 results is illustrated when mirroring the low stress regions. Rhino and Grasshopper tools lend themselves to this type of analysis. The Hausdorff distances, the intersection (∩) and union (∪) areas between two mirrored shapes, and the percentage of the intersection compared to the union area are presented in Table 6. The area data, combined with the Hausdorff distances quantify shape differences clearly (bolded text), and this data complements the common overlap percentage. Interestingly, the Y values of the centroids are close between quadrants, but there is an X value shift. This is to be explored further.

(a)

(b)
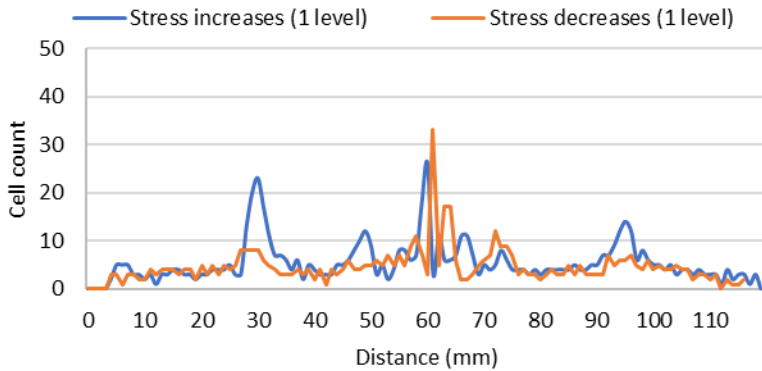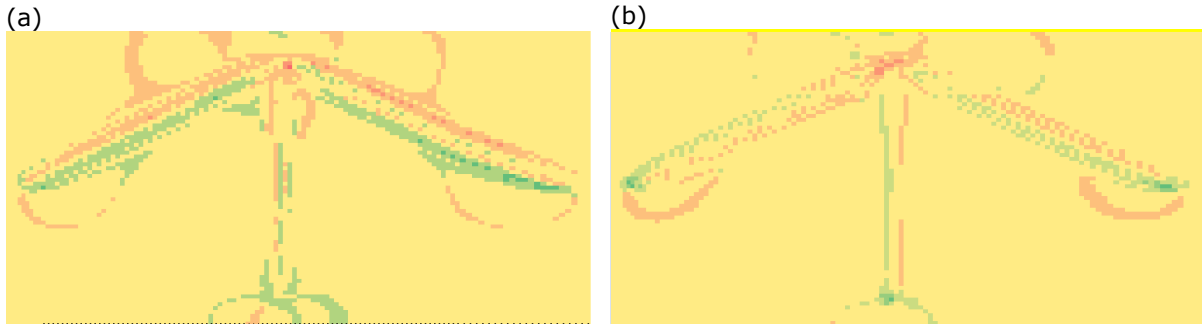
(c)
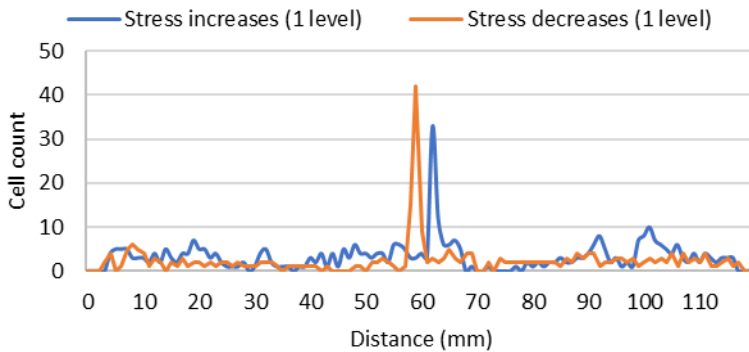
(d)

Figure 24: Difference in the XX stresses at (a) the plate top and (b) 4 mm into the plate for the radiate in (R_in) and radiate out (R_out) configurations (c) and (d) line graphs illustrating the stress level increases and decreases (1 level).

4.4   Pattern Similarity Analysis Discussion

These analyses provide additional information with respect to FEA results in compressed formats. It is well understood that residual stresses cannot be eliminated, but they can be managed. Developing build strategies to minimize residual stresses is an obvious future goal, but another option is to shift potentially problematic residual stresses into non-critical regions. Both theses discrete and geometric analysis approaches can provide insights for suitable build strategies.
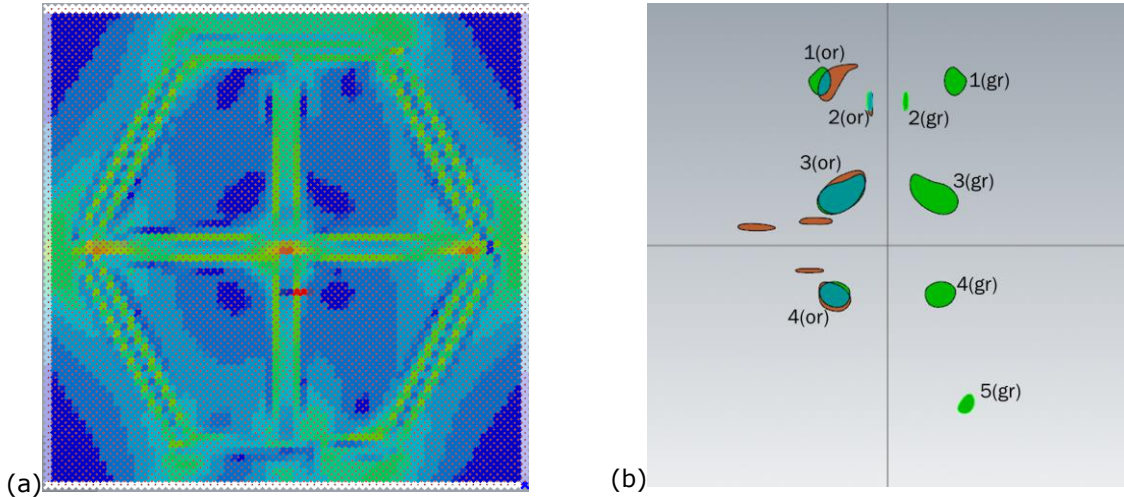
Figure 25: (a) The pixel-point data in Rhino® the plate top and (b) low stress geometry, where the green geometry is mirrored to compare it to the orange regions.

	Area (sq mm)	Centroid X (mm)	Centroid Y (mm_	Contour perimeter (mm)	Hausdorff distance (mm)	∩ area (sq mm)	U area (sq mm)	% Common Area
1(gr)	**37.9**	19.5	47.8	22.4	**8.0**	17.9	78.4	22.9%
2(gr)	7.0	5.3	42.1	12.3	2.0	100.2	122.6	81.7%
3(gr)	105.9	13.4	14.6	**39.9**	1.5	4.6	9.4	49.0%
4(gr)	52.2	15.3	-14.2	25.8	1.2	46.5	66.6	69.9%
5(gr)	19.5	23.0	-46.3	16.3	N/A	N/A	N/A	N/A
1(or)	**58.5**	-15.9	47.9	34.6				
2(or)	7.0	-4.9	41.2	14.7				
3(or)	116.9	-13.1	15.5	**40.6**				
4(or)	61.0	-15.6	-15.0	28.4				

Table 6: A summary of the symmetry/asymmetry assessment of the interior low stress regions.

The greatest challenge for this research is extracting the image data automatically. The color data within the images is not consistent. The RGB values in the reference legend for the FE simulations do not match the RGB values within the image. There are issues with RGB values at the transition zones and this is not consistent. For Fig. 26 (a), the FE legend has RGB values of 0,0, 255 for the dark blue, and the 0,142, 255 for the next lighter blue. In Table 7, select pixel RGB data is presented. In the enclose rectangle, some RGB values vary significantly at the boundary regions, and are not readily classified.

	RGB value: Legend	RGB value: Stress Region (Central)	RGB value: Stress Region (Red Box)
Dark blue	0,0, 255	0,0,191 0,0,189	0, 21, 191

Lighter blue	0,142, 255	0,0,188 0, 106, 191 0, 105, 188 0, 104, 188	0, 76, 191

Table 7: Select RGB values for the FEA image shown in Fig. 26 (a).

An untuned example is shown in Fig. 26 (b), where unknown RGB classifications are illustrated as blanks. It was found that the classification regions need to be tuned based on the general color characteristics of the image set being analyzed. The von Mises stress images have blue tones, whereas the XX, YY, ZZ residual stresses have yellow tones. Tuning the classification ranges reduced the data collection issues significantly (~ 94% good data) but did not eliminate them. Artifacts such as reference axes need to be ignored, and in complex regions such as those shown in Fig. 11 (b) require additional rules for classifications, as the RGB may values vary significantly but still convey a similar shade to the eye. More research needs to be performed for the image processing, and it is proposed to use a convolution neural network, which is applied quite frequency in image analysis applications.

(a)

(b)
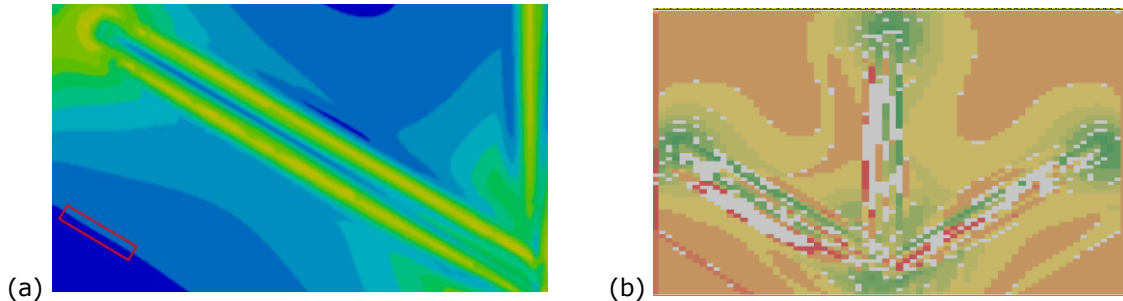
Figure 26: (a) 3 Joint (radiate out configuration) von Mises stresses, where the enclosed region has unpredictable RGB values, and (b) problematic von Mises results when comparing the top and 4 mm into the plate results.

5   SUMMARY AND CONCLUSIONS

Confidence in predicting the mechanical and physical properties for AM build components is required for this process family to expand in industry. Simulations can provide insights into the thermal-mechanical-metallurgical behaviors that experimental approaches cannot determine, but much data is not assessed (including data between the nodes). Therefore, methodologies to interpret the result patterns beyond determining maximum and minimum points or querying the properties at specific nodes needs to be developed. This has been done for both curve and pattern sets for several FE simulation scenarios.

Metrics exist to evaluate curve similarities but were found to convey limited meaning. Consequently, the offset curve capture (OCC) logic test is generated, which provides a more comprehensive assessment of closeness. This was demonstrated for several case studies but is challenging to implement without leveraging CAD tools. It would be interesting to explore the Hausdorff, NN, and K-S distances within offset curve sets, and the OCC metric for other applications.

A method to convert FEA results' images into topology and structured 'raster' data via image sampling is presented. Transforming RGB data into discrete classifications via geometry manipulation tools allows researchers to extract data that will allow for extended analyses to be

performed. For this research, von Mises and residual stress analyses for several case studies are employed to assess the goodness of this approach. Establishing Excel templates and importing the point cloud data allows for much data to be evaluated quickly and systematically. Structured graphs allow for global and local assessments. Additional analyses, such as exploring structural similarity approaches [3, 12], will be conducted now this baseline is established. Exploiting CAD tools also allowed for pattern data to be extracted.

It was found that direct image conversion approaches do not provide the expected results due to issues related to the image quality. Unexpected color variations (or noise) exist throughout the images. It is recommended to explore convolution neural network methods to extract the relevant data. This is a key issue to resolve.

To conclude, this work will facilitate with FE results interpretation and predictive model development when comparing different simulation scenarios. The techniques can be extended to a general FE post-processing module. However, CAD tools need to be intelligently integrated within the post-processing module to leverage the full potential of the simulation data.

6   ACKNOWLEDGEMENTS

(Ruth) Jill Urbanic, http://orcid.org/0000-0002-2906-7618
Bita Mohajernia, http://orcid.org/0000-0001-7119-2490

7   REFERENCES

[1]   Alt, H.; Godau, M.: Computing the Fréchet distance between two polygonal curves, Int. J. Comput. Geometry Appl. 5, 1995, 75–91, https://www.worldscientific.com/doi/abs/10.1142/S0218195995000064
[2]   Arias-González, F.; Barro, O.; del Val, F. Lusquiños, J.; Fernández-Arias, M.; Comesaña, R.; Riveiro, A.; Pou, J.: Handbooks in Advanced Manufacturing, Chapter 4 - Laser-directed energy deposition: principles and applications, 2021, 121-157. https://doi.org/10.1016/B978-0-12-818411-0.00003-3.
[3]   Attalla, E.; Siy, P.: Robust shape similarity retrieval based on contour segmentation polygonal multiresolution and elastic matching, Pattern Recognition, 38(12), 2005, 2229-2241. https://doi.org/10.1016/j.patcog.2005.02.009.
[4]   Baertsch, F.; Ameli, A.; Mayer, T.: Finite-Element Modeling and Optimization of 3D-Printed Auxetic Reentrant Structures with Stiffness Gradient under Low-Velocity Impact, Journal of Engineering Mechanics, 147(7), 2021, https://ascelibrary.org/doi/abs/10.1061/%28ASCE%29EM.1943-7889.0001923.
[5]   Buchin, M.; Kilgus, B.: Fréchet distance between two-point sets, Computational Geometry, 102, 2022. https://doi.org/10.1016/j.comgeo.2021.101842
[6]   Crispo, L.; Bohrer, R.; Roper, S.; Kim, I- Y.: Spatial gradient interface detection in topology optimization for an unstructured mesh, Struct Multidisc Optim 63, 2021, 515–522. https://doi.org/10.1007/s00158-020-02688-z.
[7]   Dokken, J.; Funke, S.; Johansson, A.; Schmidt, S.: Shape Optimization Using the Finite Element Method on Multiple Meshes with Nitsche Coupling, SIAM Journal on Scientific Computing, 41(3), 2019, A1923-A1948, https://doi.org/10.1137/18M1189208.
[8]   Filion, G.J.: The signed Kolmogorov-Smirnov test: why it should not be used, GigaSci 4 (9), 2015. https://doi.org/10.1186/s13742-015-0048-7.
[9]   GIMP Development Team, 2019, GIMP, Available at: https://www.gimp.org.

[10] Kalami, H.; Urbanic, J.: Numerical analysis of hardness variations for a dome built without supports using directed energy deposition and multi-axis tool paths, Int J Adv Manuf Technol 116(975–991), 2021. https://doi.org/10.1007/s00170-021-07504-6.

[11] Kaplan, H.; Tenenbaum, J.: Locality Sensitive Hashing for Efficient Similar Polygon Retrieval, 38th International Symposium on Theoretical Aspects of Computer Science, 2021, arXiv, https://doi.org/10.48550/arXiv.2101.04339.

[12] Magnier B.; Moradi B.: Shape Similarity Measurement for Known-Object Localization: A New Normalized Assessment. J Imaging., 5(10), 2019, 77. https://doi:10.3390/jimaging5100077.

[13] Mirazimzadeh, S.E.; Pazireh, S.; Urbanic, J.; Hedrick, B.: Investigation of effects of different moving heat source scanning patterns on thermo-mechanical behavior in direct energy deposition manufacturing, Int J Adv Manuf Technol, 2022. https://doi.org/10.1007/s00170-022-08970-2

[14] Mohajernia, B.; Urbanic, R. J.: Residual Stress Modeling of Junction Structures Using Powder Injection Laser Cladding of Martensitic Stainless Steel on Low Alloyed Carbon Steel Substrate, Computer-Aided Design and Applications, 19(6), 2022, https://doi.org/10.14733/cadaps.2022.1070-1092.

[15] Mohajernia, B.; Mirazimzadeh, S.E.; Pasha, A.; Urbanic, R. J.: Machine learning approaches for predicting geometric and mechanical characteristics for single P420 laser beads clad onto an AISI 1018 substrate, Int J Adv Manuf Technol, 118, 2022, 3691–3710. https://doi.org/10.1007/s00170-021-08155-3.

[16] Morgenstern, Y.; Hartmann, F.; Schmidt, F.; Tiedemann, H.; Prokott, E.; Maiello, G.; Fleming. R.: An image-computable model of human visual shape similarity, PLOS, Computational Biology. 17(6), 2021, e1008981. https://doi.org/10.1371/journal.pcbi.1008981.

[17] Mozaffar, M.; Ndip-Agbor, E.; Lin, S.; Wagner, G.; Ehmann, K.; Cao, J.: Acceleration strategies for explicit finite element analysis of metal powder-based additive manufacturing processes using graphical processing units, Computational Mechanics, 64(3), 2019, 879-894, https://doi.org/10.1007/s00466-019-01685-4.

[18] Nakamura, T.; Taki, K.; Nomiya, H.; Seki, K.; Uehara, K.: A shape-based similarity measure for time series data with ensemble learning. Pattern Anal Applic 16, 2013535–548, https://doi.org/10.1007/s10044-011-0262-6

[19] Nazemi, N.; Urbanic, R. J.: A numerical investigation for alternative toolpath deposition solutions for surface cladding of stainless steel P420 powder on AISI 1018 steel substrate, International Journal of Advanced Manufacturing Technology, 96/(9-12), 2018, 4123-4143. https://doi.org/10.1007/s00170-018-1840-1.

[20] Pincus Z.; Theriot JA.; Comparison of quantitative methods for cell-shape analysis, J Microsc. 227(Pt 2), 2007, 140-56. https://doi:10.1111/j.1365-2818.2007.01799.

[21] Roda-Casanova, V.; Sanchez-Marin, F.: A simple procedure for generating locally refined 2D quadrilateral finite element meshes of gears, Mechanism and Machine Theory, 157, 2021, https://doi.org/10.1016/j.mechmachtheory.2020.104185

[22] SdTC, A.: Mathematical Notation to Represent Cumulative Sum, URL (version: 2017-03-22): https://math.stackexchange.com/q/2197571.

[23] SYSWELD: ESI-Group (2020) SYSWELD 2020 reference manual

[24] Tang, L.; Zhang, X.; Kan, Z.; Li, Q.: Spatial data Internet progressive transmission control based on the geometric shapes similarity, Int. J. Control Autom. Syst. 12, 2014, 1110–1117. https://doi.org/10.1007/s12555-012-0484-4

[25] Urbanic, R. J.; Mohajernia, B.; Nazemi, N.: Developing Geometric Analysis Tools to Compare Heat Map Results for Metal Additive Manufactured Components, CAD & A, 17(2), 2019, 288-311, https://doi.org/10.14733/cadaps.2020.288-311.

[26] Zhang, X.; Liou, F.: Handbooks in Advanced Manufacturing, Chapter 1 - Introduction to additive manufacturing, Elsevier, 2021, 1-31. https://doi.org/10.1016/B978-0-12-818411-0.00009-4